

A TWO-SCALE APPROACH FOR THE DROP SHOCK SIMULATION OF PCB PACKAGE CONSIDERING THE REFLOWED SOLDER BALL GEOMETRIES

Wei Hu,¹ Xiaofei Pan,¹ Dandan Lyu,¹ Ashutosh Srivastava,² Siddharth Shah,² C. T. Wu^{1,}*

¹ *Computational and Multiscale Mechanics Group, Livermore Software Technology, An Ansys Company, Livermore, CA, USA*

² *Ansys Inc., Canonsburg, PA, USA*

In this paper, we introduce a new computational approach for linking the information of mesoscale solder ball shapes to the macroscale drop test of a printed circuit board (PCB). The approach starts with a numerical prediction of mesoscale solder bump profiles using a novel full-implicit Lagrangian particle method to approximate the Navier-Stokes equations and efficiently simulate the incompressible free surface reflow soldering process. The surface tension of the molten solder and the wall adhesion between the solder and the substrate are considered in the simulation. Subsequently, the predicted solder ball shapes from the reflow analysis are used in a chip package model for the drop shock analysis. The mesoscale solder joint model is coupled concurrently with the macroscale chip package model using the co-simulation to achieve the non-intrusive scale-bridging effect. To attend practical explicit-explicit two-scale co-simulations, an algorithm that handles properly the load-balancing, heterogeneity of processors and memory also has been developed. We present four numerical examples that showcase the effectiveness of the new approach.

KEY WORDS: *particle method, solder ball, Navier-Stokes, co-simulation, multiscale model*

1. INTRODUCTION

Due to the toxicity of lead (Pb), lead-free solder joint (Chong et al., 2006) has become the main mechanical and electrical connection in modern microelectronics packaging for almost every electronic product for the purpose of environmental friendliness. However, lead-free solders are more brittle in nature due to stiffness and excessive intermetallic compounds growth at the solder joint to pad interface (Ma and Lee, 2013). This gives rise to a higher risk of solder joints failures. While hundreds of lead-free solder joints are used for interconnection in microelectronics packaging, they are often considered the weakest points as regards to structural strength in the drop test. If one solder joint fails in a PCB, the whole electronic system may break down. As hand-held electronic devices such as cellular phones are prone to drop, the drop shock reliability and failure analysis of lead-free solder joints has become critical in the electronic product design and engineering. Therefore, during the product's virtual development process, extensive computer simulations

*Address all correspondence to C. T. Wu, E-mail: ct.wu@ansys.com

of drop test are conducted using commercial explicit finite element codes such as LS-DYNA and ABAQUS to study the drop shock response of the solder joints before the designed printed circuit board (PCB) and electronic assembly are ready for production.

In the board-level drop test, the shape of the solder ball is a very important contributory factor (Grovenor, 2017) in determining the local stress levels. It has been observed in experiments (Chiang et al., 2000; Chiang and Yuan, 2001) that solder joint reliability is highly depending on the geometry of solder ball including the standoff height, maximum solder ball width and contact angle between solder and substrate. The solder ball is formed during a reflow process. When the solder paste reaches the eutectic temperature in the reflow, the solder alloy undergoes a phase change to a liquid or molten state. Since the molten solder alloy in reflow behaves like water with properties of cohesive and adhesion, the surface tension of the molten solder and the wall adhesion between the solder and the substrate will have to be considered in order to obtain the right solder ball shape and contact angle (Chou et al., 2006) in the numerical simulation. Nevertheless, the computational fluid dynamics (CFD) methods based on the Eulerian approach and free-surface tracking techniques such as level set and volume of fluid method (Rodrigues et al., 2016) are prohibitive expensive to compute the evolving solder surface in three-dimensional space. As a consequence, they are not commonly used for the prediction of solder reflow profile in a variety of packages such as the ball grid array (BGA) package. Without taking into account the wall adhesion effect, the geometrically-based truncated sphere theory (Chiang and Yuan, 2001), force-balanced analytical methods (Heinrich et al., 1996) and their combination with finite element method (Amalu and Ekere, 2012) have been used with the design of experiment (DOE) methodology to efficiently predict the solder ball shape in the package design. To further obtain the solder contact angle, the energy-based Surface Evolver tool (Brakke, K. A., 1996; Yeung and Lee, 2003) has become popular to study the molten solder surfaces shaped by the surface tension and adhesion force. However, the Surface Evolver has strong restrictions in considering the solder mask and modeling the overflow (Chou et al., 2006). While using the experimental measurement to obtain all solder ball geometries is impractical, the electronics industry demands a general-purpose tool for the prediction of solder ball shape and contact angle in the solder joint design as well as for the drop test simulation.

In a drop shock event, the stress wave is transmitted from the PCB to the integrated circuit (IC) chip through the solder joints. Modeling the mesoscale solder joint in chip-scale packages (CSPs) under dynamic loading and impact conditions is challenging in terms of computational efficiency. This is due to the very small time step in traversing the stress waves through the smallest-size element limited by the CFL (Courant-Friedrichs-Lewy) courant condition in the explicit dynamic analysis. The numerical simulation involves modeling the drop shock effect on mesoscale solder joints and macroscale chip packages concurrently, which is a typical multiscale problem. Unfortunately, the current state-of-the-art finite element methods and sub-modeling techniques (Yu et al., 2012) are difficult to model this two-scale problem accurately and efficiently.

There are several crucial numerical obstacles to overcome in the CSPs drop test simulation. First of all, conventional approaches using beam element (Kok et al., 2016) are efficient but insufficient to model realistic reflowed solder joint geometry and its structural behavior. Therefore, modeling the mesoscale solder ball using solid elements is necessary. Secondly, multiple solder balls on PCB should be modeled as an in-homogeneous group with non-identical reflowed geometries from an accuracy point of view. In other words, each solder should have its own ball shape and contact angle depending on the positions of the balls on PCB, substrate configuration and soldering conditions. For example, the thermal-induced PCB warpage may cause out-of-plane alignment of solder bumps, leading to different final shapes of reflowed solder

joints (Rayasam et al., 2006; Xia et al., 2014). For an accurate simulation, one cannot simply calculate a single solder reflow profile and apply it to multiple solder balls at different solder joint positions. To improve the solder joint reliability study in the drop test simulation, a board-level solder joint model containing dissimilar reflowed solder ball geometries is desired. Thirdly, the conventional sub-modeling technique (Yu et al., 2012) developed for drop shock analysis is based on the one-way (information exchange only in one direction from macroscale to mesoscale levels) coupling technique, which is efficient but less accurate. Although the sub-cycling technique (Chong et al., 2006) is more accurate than the sub-modeling, it is computationally intensive and difficult to be used in the structure failure analysis. It is also non-trivial for the sub-cycling technique to implement an effective domain-decomposition for the multi-chip problem, thus the technique is not commonly used in practice. **As the computational efficiency is the main issue in this type of simulation, the integration of advanced numerical techniques with modern computer infrastructures has driven the research and software development for efficient multiscale analysis.**

The objective of this study is to develop a new computational approach **via a co-simulation technique** that addresses the three critical needs in higher-level modeling of chip scale drop tests. In essence, an effective modeling of drop shock reliability of solder joints demands an accurate solder ball reflow simulation using a solid element formulation for the prediction of mesoscale solder ball geometry as well as a meso-macroscale coupling method for the explicit dynamics analysis. The remainder of the paper is organized as follows: In Section 2, a full-implicit incompressible smoothed particle Galerkin (ISPG) method is introduced to model the solder reflow process and predict the solder ball shape. The formulation considering the surface tension of molten solder and the wall adhesion between the solder and the substrate is provided. Section 3 describes the explicit-explicit non-intrusive two-scale coupling method and its weak formulation for the drop test simulation. The data exchange and its implementation procedures **for the co-simulation** are provided in the same section. Four numerical examples are given in Section 4, and conclusions are made in Section 5.

2. A FULL-IMPLICIT ISPG FORMULATION WITH SURFACE TENSION AND ADHESION EFFECTS

Incompressible smoothed particle Galerkin (ISPG) method (Pan et al., 2020) is a semi-implicit fluid-dynamics version of smoothed particle Galerkin (SPG) method (Wu et al., 2017; Wu et al., 2018). SPG method was initially introduced for the large deformation and material failure analysis in the solid mechanics applications. As one of the new CFD methods, ISPG method differs from others in several important aspects. Unlike Eulerian finite element or finite volume methods, ISPG method solves the Navier-Stokes equation in a Lagrangian fashion for free surface fluid flow problems. This eliminates the need of using the expensive surface-tracking techniques to locate the free surface. ISPG method utilizes a momentum-consistent velocity smoothing algorithm (Pan et al., 2019; Wu et al., 2020) from SPG method to stabilize the velocity field. This is different from existing Lagrangian particle methods such as incompressible smoothed particle hydrodynamics (ISPH) (Asai et al., 2012) and moving particle semi-implicit method (MPS) (Koshizuka and Oka, 1996) which usually rely on *ad hoc* techniques based on particle shifting, artificial viscosity or density-invariant conditions for stabilization (Pan et al., 2020). ISPG also incorporates a pressure **correction** method which employs a second-order rotational incremental pressure-correction scheme (Guermond et al., 2006) to stabilize the pressure field and to enforce the consistency of Neumann boundary condition; see e.g., (Pan et al., 2020) for the ISPG method in detail.

In order to model the solder reflow process more efficiently and accurately than the semi-implicit ISPG method, a full-implicit ISPG method is developed in this study. Additionally, we supplement the full-implicit ISPG formulation with the surface tension for molten solder. We also consider the wall adhesion between the solder and the substrate to better predict the reflowed solder ball shape.

2.1 Governing Equation

The lead-free solder reflows at a fixed temperature near the solder melting (eutectic) point. Therefore, the reflow process inside the solder oven is usually considered in an isothermal state. In numerical simulation, this fluid-like solder reflow behavior is described by the Navier-Stokes equation. In this paper, the Lagrangian Navier-Stokes equation is used to describe the free surface reflow process where the governing equation comprising of the pressure term, the viscosity term and the gravity term can be written as

$$\frac{D\mathbf{v}}{Dt} = -\frac{1}{\rho}\nabla p + \frac{\vartheta}{\rho}\nabla^2\mathbf{v} + \mathbf{g} \quad (1)$$

where \mathbf{v} , ρ , p are fluid velocity, density and pressure, respectively. ϑ is the dynamic viscosity, t denotes the time, and \mathbf{g} is the gravity. The incompressible condition is enforced using the continuity equation in a standard way and is given by:

$$\nabla \cdot \mathbf{v} = 0 \quad (2)$$

2.2 Projection Scheme for Incompressible Flows

It is well-understood that numerical instability arises in the numerical simulation of incompressible flows when the velocity and the pressure are coupled by the incompressibility constraint. To overcome this numerical issue, the 2nd order generalized rotational incremental pressure-correction scheme (Guermond et al., 2006) is implemented as a fractional step method for the reflow study. In the first sub step of the 2nd order GRIPC scheme, we have

$$\frac{1}{\Delta t}(\mathbf{v}^{n+1*} - \mathbf{v}^n) = -\frac{1}{\rho}\nabla p^n + \frac{\vartheta}{\rho}\nabla^2\mathbf{v}^{n+1*} + \mathbf{g}, \quad \mathbf{v}^{n+1*}|_{\Gamma_v} = \bar{\mathbf{v}} \quad (3)$$

where \mathbf{v}^{n+1*} is the intermediate velocity, and $\bar{\mathbf{v}}$ is the wall (substrate) velocity. In the second sub step of the 2nd order GRIPC scheme, the velocities are corrected through the following equation

$$\frac{1}{\Delta t}(\mathbf{v}^{n+1} - \mathbf{v}^{n+1*}) + \frac{1}{\rho}\nabla\phi^{n+1} = 0, \quad \mathbf{v}^{n+1}|_{\Gamma_v} = \bar{\mathbf{v}} \quad (4)$$

where the variable ϕ is defined as

$$\phi^{n+1} = p^{n+1} - p^n + \vartheta\nabla \cdot \mathbf{v}^{n+1*} \quad (5)$$

The corrected velocity in Eq. (4) must satisfy the divergence-free condition, which yields the following Poisson equation,

$$\nabla \cdot \mathbf{v}^{n+1*} = \frac{\Delta t}{\rho} \nabla^2 \phi^{n+1} \quad (6)$$

From Eq. (4), it's observed that the Neumann boundary condition $\nabla \phi^{n+1} \cdot \mathbf{n}|_{\Gamma_p} = 0$. The Dirichlet boundary condition at the free surface can be induced from Eq. (5), that is

$$(\phi^{n+1} + p^n - \vartheta \nabla \cdot \mathbf{v}^{n+1*})|_{\Gamma_p} = p^{\text{fs}} \quad (7)$$

where Γ_p is the free surface boundary, and p^{fs} is the pressure at the free surfaces.

2.3 Surface Tension

During the reflow process, the surface tension causes a pressure jump $\sigma_\kappa^{\text{fs}}$ at the interface between the liquid solder and air proportional to the mean curvature of the interface

$$\sigma_\kappa^{\text{fs}} = \gamma \kappa \quad (8)$$

where γ is the surface tension coefficient, and $\kappa = -\nabla \cdot \mathbf{n}$ is the mean curvature, and \mathbf{n} is the inward normal direction of the liquid solder surface. Subsequently, the pressure term applied at the essential pressure boundary condition can be calculated as

$$p^{\text{fs}} = p^{\text{air}} + \sigma_\kappa^{\text{fs}} \quad (9)$$

where p^{air} is the air pressure. The surface tension will work against the earth's gravity during the solder reflow process.

2.4 Wall Adhesion

When molten solder is in contact with the substrate, the solder liquid interface forms a contact angle θ with the wall boundary. If the angle θ is equal to static contact angle θ_{eq} , a state of static equilibrium is reached. If not, then a nonzero wall adhesion force tends to pull the interface to the equilibrium position. In our algorithm, the wall adhesion boundary condition can be expressed by the unit free surface normal \mathbf{n} at the interface point \mathbf{x}_w shown in Fig. 1.

$$\mathbf{n}(\mathbf{x}_w) = \mathbf{n}_w \cos(\theta_{\text{eq}}) + \mathbf{t}_w \sin(\theta_{\text{eq}}) \quad (10)$$

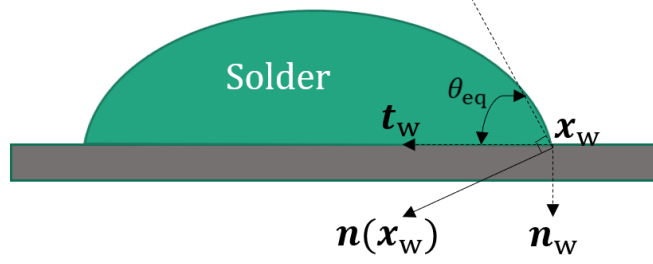


FIG. 1: Illustration of the wall adhesion

2.5 Incompressible Momentum-consistently Smoothed Lagrangian Particle Formulation

Using the 2nd order generalized rotational incremental pressure-correction scheme, the weak form of incompressible flow problem can be formulated within the Galerkin framework using the Lagrangian approach and the particle approximation.

2.5.1 Particle Approximation Function

With a particle distribution denoted by an index set $Z_I = \{\mathbf{x}_I\}_{I=1}^{N^P} \in R^3$, the displacement function $\mathbf{u}(\mathbf{x})$ can be approximated using the meshfree or particle approximation

$$\mathbf{u}^h(\mathbf{x}) = \sum_{I \in Z_I} \Psi_I^a(\mathbf{x}) \mathbf{u}_I \quad \forall \mathbf{x} \in \Omega \quad (11)$$

where N^P is the total number of particles in the discretization. $\Psi_I^a(\mathbf{x}), I = 1, \dots, N^P$ can be interpreted as the shape functions of the approximation for the field \mathbf{u}^h where the superscript “a” denotes the support size of $\Psi_I^a(\mathbf{x})$. The moving least-square interpolation with the first-order basis is used in this work.

2.5.2 Particle Discretization in the Velocity-Prediction Step

The weak form of Eq. (3) using Eq. (11) and the direct nodal integration (DNI) scheme (Wu et al., 2017) gives the following discrete equations

$$\begin{aligned} & \frac{1}{\Delta t} \sum_{K \in Z_I} \hat{m}_K \Psi_I^a(\mathbf{x}_K) \sum_{J \in Z_I} \Psi_J^a(\mathbf{x}_K) v_{ji}^{n+1*} - \frac{1}{\Delta t} \sum_{K \in Z_I} \hat{m}_K \Psi_I^a(\mathbf{x}_K) \hat{v}_{ki}^n \\ & = -\frac{1}{\rho} \sum_{K \in Z_I} \hat{m}_K \Psi_I^a(\mathbf{x}_K) \sum_{J \in Z_I} \Psi_{j,i}^a(\mathbf{x}_K) p_j^n \\ & + \frac{\vartheta}{\rho} \sum_{K \in Z_I} \hat{m}_K \Psi_I^a(\mathbf{x}_K) \sum_{J \in Z_I} \sum_{j=1}^{\text{ndim}} \Psi_{j,j}^a(\mathbf{x}_K) v_{ji}^{n+1*} + \sum_{K \in Z_I} \hat{m}_K \Psi_I^a(\mathbf{x}_K) g_i \end{aligned} \quad (12)$$

where \hat{m}_K is the mass the of particle K , and \hat{v}_{Ki}^n is i -component of unsmoothed velocity (Pan et al., 2020) of particle K . In Eq. (12) $i, j = 1, 2, 3$ for 3D (ndim = 3) and 1, 2 for 2D (ndim = 2). Alternatively, Eq. (12) can be expressed by the matrix form given by

$$\left(\frac{1}{\Delta t} \mathbf{M}^{n+1} + \mathbf{K}_i^{n+1}\right) \mathbf{V}_i^{n+1*} = \frac{1}{\Delta t} \mathbf{P}_i^n + \mathbf{F}_i^{p,n} + \mathbf{F}_i^{g,n+1} \quad (13)$$

where

$$M_{IJ}^{n+1} = \sum_{K \in Z_I} \hat{m}_K \Psi_I^a(\mathbf{x}_K) \Psi_J^a(\mathbf{x}_K) \quad (14)$$

$$P_{ii}^n = \sum_{K \in Z_I} \hat{m}_K \Psi_I^a(\mathbf{x}_K) \hat{v}_{Ki}^n \quad (15)$$

$$K_{IJ}^{n+1} = -\frac{\vartheta}{\rho} \sum_{K \in Z_I} \hat{m}_K \Psi_I^a(\mathbf{x}_K) \sum_{j=1}^{\text{ndim}} \Psi_{J,jj}^a(\mathbf{x}_K) \quad (16)$$

$$F_{ii}^{p,n+1} = -\frac{1}{\rho} \sum_{K \in Z_I} \hat{m}_K \Psi_I^a(\mathbf{x}_K) \sum_{J \in Z_I} \Psi_{J,i}^a(\mathbf{x}_K) p_J^n \quad (17)$$

$$F_{ii}^{g,n+1} = \sum_{K \in Z_I} \hat{m}_K \Psi_I^a(\mathbf{x}_K) g_i \quad (18)$$

The predicted velocity is adjusted at the solid boundaries to ensure the velocity boundary condition in Eq. (3) is satisfied, where the detail can be found in (Pan et al., 2020).

2.5.3 Solution of Poisson Equation with the 2nd Order GRIPC Scheme

The pressure field $p^h(\mathbf{x})$ and the variable $\phi^h(\mathbf{x})$ defined in Eq. (5) are approximated by the meshfree/particle approximation, that is

$$p^h(\mathbf{x}) = \sum_{I \in Z_I} \Psi_I^a(\mathbf{x}) p_I \quad \forall \mathbf{x} \in \Omega \quad (19)$$

$$\phi^h(\mathbf{x}) = \sum_{I \in Z_I} \Psi_I^a(\mathbf{x}) \phi_I \quad \forall \mathbf{x} \in \Omega \quad (20)$$

where p_I and ϕ_I are nodal coefficients for pressure and ϕ at the particle I .

To enforce different boundary conditions, particles are divided into three groups:

- 1) Interior particles, for which the Poisson equation (6) is employed, that is

$$\frac{\Delta t}{\rho} \sum_i^{\text{ndim}} \Psi_{J,ii}^a(\mathbf{x}_I) \phi_j^{n+1} = \sum_i^{\text{ndim}} \Psi_{J,i}^a(\mathbf{x}_I) v_{ji}^{n+1*}. \text{ndim} = 2 \text{ for 2D, and 3 for 3D} \quad (21)$$

2) Free surface particles, for which the Dirichlet boundary condition (7) is employed, that is

$$\Psi_j^a(\mathbf{x}_I) \phi_j^{n+1} + \Psi_j^a(\mathbf{x}_I) p_j^n - \vartheta \sum_i^{\text{ndim}} \Psi_{J,i}^a(\mathbf{x}_I) v_{ji}^{n+1*} = p^{fs}(\mathbf{x}_I) \quad (22)$$

3) Neumann boundary particles, for which the Neumann boundary condition $\nabla \phi^{n+1} \cdot \mathbf{n}|_{\Gamma_p} = 0$ is employed, that is

$$\sum_i^{\text{ndim}} n_i(\mathbf{x}_I) \Psi_{J,i}^a(\mathbf{x}_I) \phi_j^{n+1} = 0 \quad (23)$$

where $\mathbf{n}(\mathbf{x}_I)$ is the outward normal direction of the fluid at the Neumann particle I . Using Eqs. (21)-(23), the ϕ_j^{n+1} can be solved. Subsequently, the pressure field $p^h(\mathbf{x})$ at the time step $n + 1$ can be obtained through Eq. (5), that is

$$p^{h,n+1}(\mathbf{x}) = \sum_{J \in Z_I} \Psi_J^a(\mathbf{x}) \phi_J^{n+1} + \sum_{J \in Z_I} \Psi_J^a(\mathbf{x}) p_J^n - \vartheta \sum_i^{\text{ndim}} \sum_{J \in Z_I} \Psi_{J,i}^a(\mathbf{x}) v_{ji}^{n+1*} \quad (24)$$

Their values at the particles are used as particle coefficients of pressure p^{n+1} for the computation in the next time step.

2.5.4 Particle Discretization in the Velocity-Correction Step with the 2nd Order GRIPC Scheme

By employing the meshfree/particle shape function and the direct nodal integration DNI scheme, Eq. (4) becomes

$$\frac{\mathbf{M}^{n+1}}{\Delta t} (\mathbf{V}_i^{n+1} - \mathbf{V}_i^{n+1*}) = \mathbf{F}_i^{\phi,n+1}. \quad i = 1,2,3 \text{ for 3D and } 1,2 \text{ for 2D} \quad (25)$$

where

$$\mathbf{F}_i^{\phi,n+1} = -\frac{1}{\rho} \sum_{K \in Z_I} \hat{m}_K \Psi_I^a(\mathbf{x}_K) \sum_{J \in Z_I} \Psi_{J,i}^a(\mathbf{x}_K) \phi_J^{n+1}$$

The consistent mass matrix in Eq. (25) can be replaced by the lumped mass matrix, in which only the diagonal element is non-zero. Thus Eq. (25) becomes

$$\frac{\mathbf{M}^{\text{lump},n+1}}{\Delta t} (\mathbf{V}_i^{n+1} - \mathbf{V}_i^{n+1*}) = \mathbf{F}_i^{\phi,n+1}. \quad i = 1,2,3 \text{ for 3D and } 1,2 \text{ for 2D} \quad (26)$$

where the particle velocity at time step $n + 1$ can be explicitly computed and corrected.

2.6 Updating the Velocities and Positions of the Lagrangian Particles

After particle velocities are corrected, particles move with corrected particle velocities, that is

$$\mathbf{x}_j^{n+1} = \mathbf{x}_j^n + \Delta t \sum_{I \in Z_I} \psi_I^a(\mathbf{x}_j) \mathbf{v}_I^{n+1} \quad (27)$$

The unsmoothed value of particle velocities should be updated for the computation in the next time step using the following equation,

$$\hat{\mathbf{v}}_j^{n+1} = (1 - \alpha) \left(\hat{\mathbf{v}}_j^n + \sum_{I \in Z_I} \psi_I^a(\mathbf{x}_j) (\mathbf{v}_I^{n+1} - \mathbf{v}_I^n) \right) + \alpha \sum_{I \in Z_I} \psi_I^a(\mathbf{x}_j) \mathbf{v}_I^{n+1} \quad (28)$$

Here α is the relaxation factor to control the numerical dissipation (Idelsohn et al., 2004) given by

$$\Delta E(\alpha) = -\alpha(2 - \alpha) \frac{1}{2} \sum_{I \in Z_I} \hat{m}_I \left(\hat{\mathbf{v}}_I - \sum_{J \in Z_I} \psi_I^a(\mathbf{x}_J) \mathbf{v}_J \right) \quad (29)$$

By varying α from 0 to 1, one can change the amount of dissipation introduced in the system. In our simulations, α is taken as 0.5.

2.7 Fluid-Structure Coupling

Usually the solder reflowing process takes several minutes, and the implicit approach should be used in the structural analysis for the efficiency reason. A coupling algorithm between the implicit ISPG solver and the implicit structure solver is developed, which is summarized in a flowchart shown in Fig. 2.

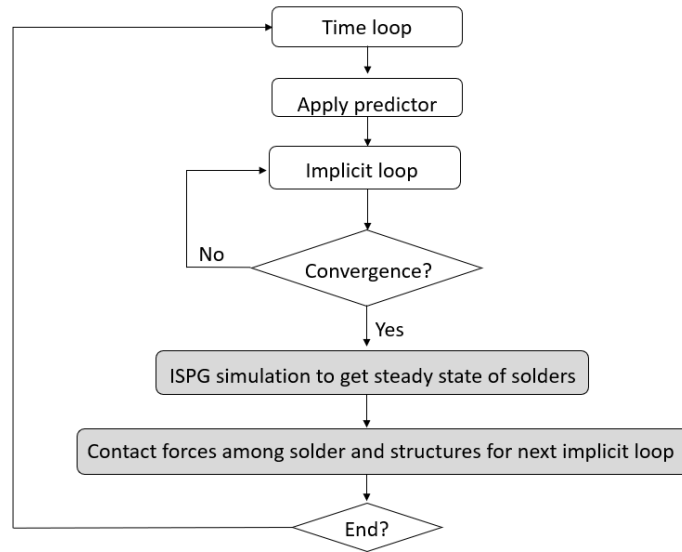


FIG. 2: Flow chart for coupling of the ISPG solver and implicit structure solver

3. TWO-SCALE CO-SIMULATION FOR DROP TEST SIMULATION

Many concurrent multiscale methods have been developed utilizing different bridging domain techniques (Dhia and Rateau, 2005; Sun et al., 2020) for coupling continuum-continuum or continuum-discrete models. In transient dynamic systems, one of the issues in multiscale concurrent coupling is in tailoring the time step to meet the efficient computation. This section describes a two-scale coupling method that incorporates the reflowed solder joints with the chip package using the co-simulation for an efficient drop test simulation. This is a type of concurrent multiscale methods (Gendre et al., 2009) known as the non-intrusive approach where data exchanges between mesoscale solder joints and the macroscale chip package concern only nodal forces and velocities in the interface zone.

The earlier developments of two-scale coupling method for transient dynamic problems can be traced back to the work of Belytschko (Belytschko et al., 1979) in sub-cycling. Sub-cycling is based on the domain decomposition technique where the coupling between the subdomains is ensured by the continuity of velocities at their interface. The dynamic Large Time Increment (LATIN) method (Boucard et al., 2011) is another multiscale coupling strategy also based on the domain decomposition technique. The LATIN method introduced a multi-parametric strategy which deals with not only the velocities but also the forces at the interfaces between the different subdomains simultaneously. Coupling methods based on the domain decomposition technique share a common feature in employing the non-overlapping mesh to interface subdomains.

Different from the classical two-scale coupling method, co-simulation (Dehning et al., 2015) often refers to a numerical approach coupling different subsystems of a model and simulating them in a distributed manner. It combines two or more separate analyses using same or different simulation codes and runs at different time scales. In literatures, co-simulation is often used to solve the multi-physics problems through implicit-implicit or implicit-explicit coupling of solvers. Recently, co-simulation also has been combined with the domain decomposition technique to solve the multiscale problems using the explicit-explicit coupling in transient dynamic analysis. Several global-local methods employing different data exchanges techniques (Bettinotti et al., 2017; Ahmed and Xue, 2020) have been developed to substantially reduce the computational cost of explicit dynamic analysis in co-simulation.

3.1 Weak Formulation of the Two-Scale Coupling System

In a two-scale coupling system, the variational equations for a transient dynamic problem can be formulated using the integration by part to find the macroscale (global) displacement field $\mathbf{u}^G(\mathbf{X}^G, t) \in V^G = \{\mathbf{u}^G \in H^1(\Omega^G); \mathbf{u}^G = \mathbf{u}_g \text{ on } \partial\Omega_g\}$ and the mesoscale (local) displacement field $\mathbf{u}^L(\mathbf{X}^L, t) \in V^L = \{\mathbf{u}^L \in H^1(\Omega^L); \mathbf{u}^L = \mathbf{u}^G \text{ on } \partial\Omega_c\}$, such that for arbitrary variation $\delta\mathbf{u}^G \in V_0^G = \{\mathbf{u}^G \in H^1(\Omega^G); \mathbf{u}^G = 0 \text{ on } \partial\Omega_g\}$ and $\delta\mathbf{u}^L \in V_0^L = \{\mathbf{u}^L \in H^1(\Omega^L); \mathbf{u}^L = 0 \text{ on } \partial\Omega_c\}$, the following equations are satisfied:

$$\int_{\Omega^G} \rho \ddot{\mathbf{u}}^G \cdot \delta\mathbf{u}^G d\Omega + \int_{\Omega^G} \boldsymbol{\sigma} : \nabla^s(\delta\mathbf{u}^G) d\Omega = \int_{\Omega^G} \mathbf{b} \cdot \delta\mathbf{u}^G d\Omega + \int_{\partial\Omega_n} \mathbf{h} \cdot \delta\mathbf{u}^G ds + \int_{\partial\Omega_c} \mathbf{f}^c \cdot \delta\mathbf{u}^G ds \quad (30)$$

$$\int_{\Omega^L} \rho \ddot{\mathbf{u}}^L \cdot \delta \mathbf{u}^L d\Omega + \int_{\Omega^L} \boldsymbol{\sigma} : \nabla^s (\delta \mathbf{u}^L) d\Omega = 0 \quad (31)$$

where Ω^G and Ω^L denote the macroscale and mesoscale domains, respectively. \mathbf{b} is the body force vector and $\boldsymbol{\sigma}$ is the Cauchy stress obtained from the constitutive law. The $\partial\Omega_g$ notation describes a Dirichlet boundary imposed by a displacement \mathbf{u}_g and $\partial\Omega_n$ is the Neumann boundary prescribed by a surface traction \mathbf{h} with $\partial\Omega_g \cap \partial\Omega_n = \emptyset$. $\partial\Omega_c$ is the coupling interface of two scales as shown in Fig. 3, where the kinematic constraint equations $\mathbf{u}^L = \mathbf{u}^G$, $\dot{\mathbf{u}}^L = \dot{\mathbf{u}}^G$ are imposed in the mesoscale computation and \mathbf{f}^c is the constrained force computed from the mesoscale.

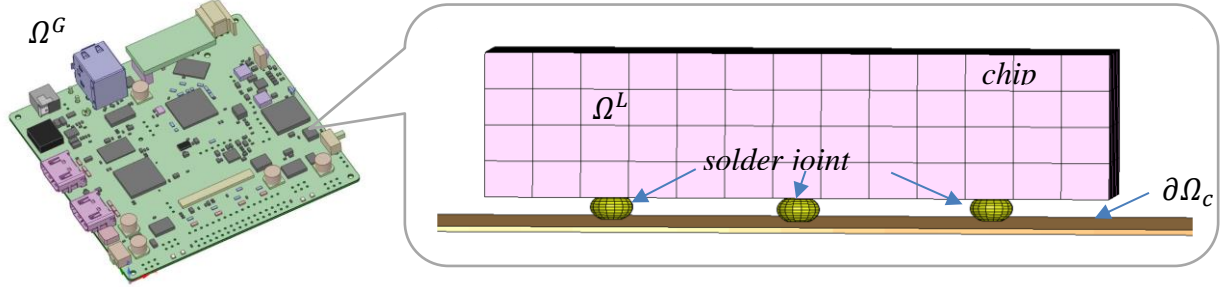


FIG. 3: Two-scale models of solder joints in large scale structure

By substituting the FEM approximations $\mathbf{u}^G(\mathbf{X}^G, t) = \sum_I N_I^G(\mathbf{X}^G) \mathbf{U}_I^G(t)$, $\mathbf{u}^L(\mathbf{X}^L, t) = \sum_I N_I^L(\mathbf{X}^L) \mathbf{U}_I^L(t)$ into Eqs. (30) and (31), the semi-discrete equations can be expressed by the following algebraic equations

$$\mathbf{M}^G \ddot{\mathbf{U}}^G = \mathbf{F}^{ext} + \mathbf{F}^c - \mathbf{F}_{int}^G \quad (32)$$

$$\mathbf{M}^L \ddot{\mathbf{U}}^L = -\mathbf{F}_{int}^L \quad (33)$$

where

$$\mathbf{M}_{IJ}^G = \int_{\Omega^G} \rho N_I^G N_J^G \mathbf{I} d\Omega \quad (34)$$

$$\mathbf{F}_I^{ext} = \int_{\Omega^G} \mathbf{b} N_I^G J_0 d\Omega + \int_{\partial\Omega_n} \mathbf{h} N_I^G ds \quad (35)$$

$$\mathbf{F}_I^c = \int_{\partial\Omega_c} \mathbf{f}_I^c ds \quad (36)$$

$$\mathbf{F}_{int,I}^G = \int_{\Omega^G} \boldsymbol{\sigma}_0 : \nabla_{\mathbf{X}^G} N_I^G d\Omega \quad (37)$$

$$\mathbf{M}_{IJ}^L = \int_{\Omega^L} \rho N_I^L N_J^L \mathbf{I} d\Omega \quad (38)$$

$$\mathbf{F}_{int,I}^L = \int_{\Omega^L} \boldsymbol{\sigma}_0 : \nabla_{\mathbf{X}^L} N_I^L d\Omega \quad (39)$$

where N^G and N^L are approximation functions in the macro and meso scales, respectively. $\boldsymbol{\sigma}_0$ is the first Piola-Kirchhoff stress tensor.

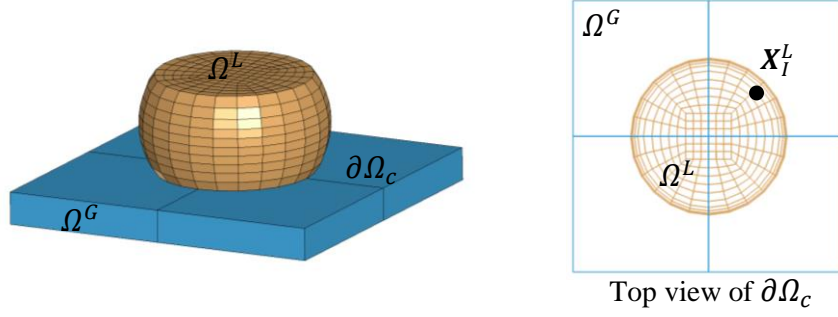


FIG. 4: The non-conforming coupling interface between macroscale and mesoscale mesh

Considering the non-conforming mesh shown in Fig. 4 at the interface across two scales, the kinematic constraints in the mesoscale are approximated as follows:

$$\mathbf{U}_I^L \equiv \mathbf{U}^L(\mathbf{X}_I^L) = \sum_J N_J^G(\mathbf{X}_I^L) \mathbf{U}_J^G, \text{ for } \forall \mathbf{X}_I^L \in \partial\Omega_c \quad (40)$$

$$\dot{\mathbf{U}}_I^L \equiv \dot{\mathbf{U}}^L(\mathbf{X}_I^L) = \sum_J N_J^G(\mathbf{X}_I^L) \dot{\mathbf{U}}_J^G, \text{ for } \forall \mathbf{X}_I^L \in \partial\Omega_c \quad (41)$$

The constrained force can be computed by integrating all the contribution from the mesoscale internal force at the coupling interface $\partial\Omega_c$ as follows:

$$\mathbf{F}_I^c \equiv \mathbf{F}^c(\mathbf{X}_I^G) = \sum_J N_I^G(\mathbf{X}_I^G) \mathbf{F}_{int,J}^L, \text{ for } \forall \mathbf{X}_I^G \in \partial\Omega_c \quad (42)$$

3.2 MPI Data Exchange and Numerical Procedure of Co-Simulation

Apparently, the critical time step in Δt^L needed in Eq. (33) of mesoscale solder joints model will be much smaller than Δt^G required in Eq. (32) of macroscale chip package model. Therefore, instead of imposing the same small time step size on the whole structure, we isolate the computation in mesoscale model but make it run simultaneously with macroscale structures using the co-simulation.

The co-simulation is performed using global/local setup, where the collective communication between global and local jobs is carried out at synchronization points currently through MPI. An adaptor is called by two local jobs to exchange data and synchronize the time integration so that the main structure of existing finite element code needs no change to be adopted in both jobs. Fig. 5 shows the flowchart of proposed co-simulation using central difference time integration scheme.

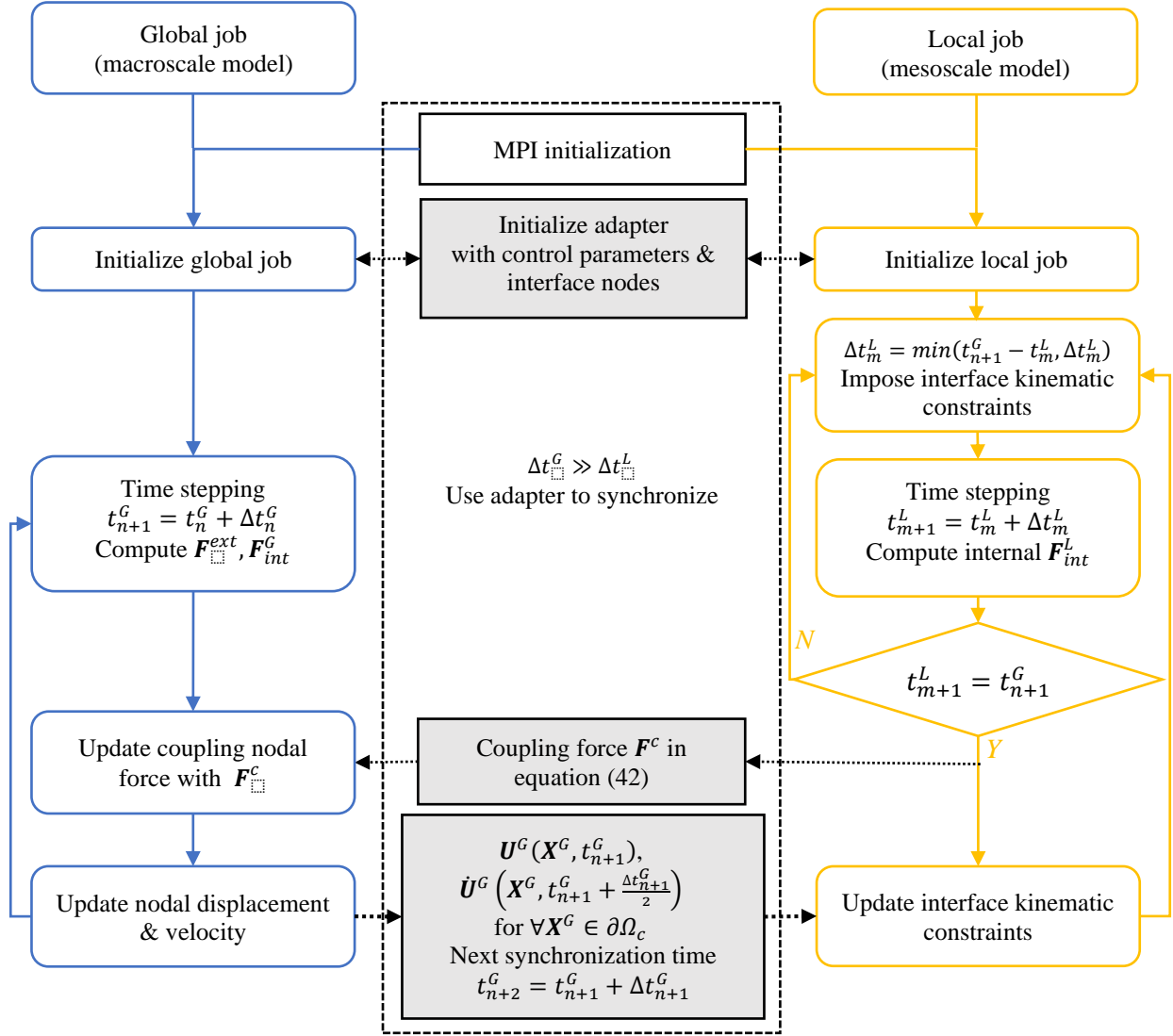


FIG. 5: The co-simulation flowchart

4. NUMERICAL EXAMPLES

4.1 Shape Prediction of Solder Joint with Fixed Contact Angles

In this example, the shape evolution of a cubic solder is simulated, and its final size is compared with the analytical solution. The original size of the cubic solder is $1\text{mm} \times 1\text{mm} \times 1\text{mm}$. The density and surface tension of the solder are $8.93 \times 10^{-6}\text{g}/\text{mm}^3$ and $4.985 \times 10^{-6}\text{kN}/\text{mm}$, respectively. The solder is discretized with 11 nodes in every direction shown in Fig. 6, which leads to a model having a total of 1331 particles. For the contact between solder and pad, the free-slip boundary condition is applied. Two

equilibrium contact angles $\pi/6$ and $\pi/3$ are used separately for the simulation. No gravity is considered in this study, and the total simulation time is 100ms.

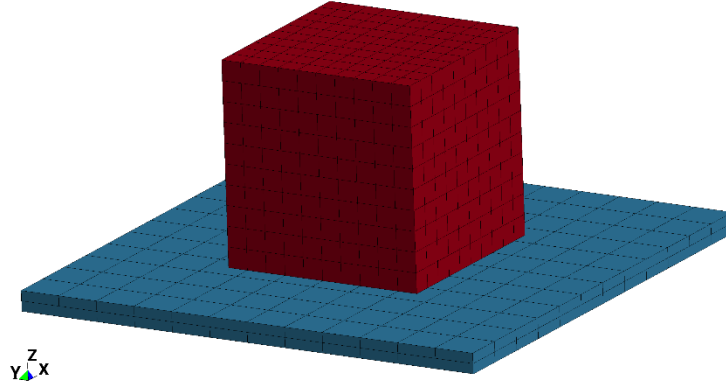


FIG. 6: Discretization of the solder and pad

Figs. 7(a) and (b) give the final equilibrium configuration of the solder with the equilibrium contact angles $\pi/6$ and $\pi/3$, respectively. The comparison of final height and width is summarized in Table 1 and Table 2. The difference between the predicted size and the analytical solution with truncated sphere theory (Chiang and Yuan, 2001) is smaller than 5%, despite a very coarse resolution is used in our simulations.

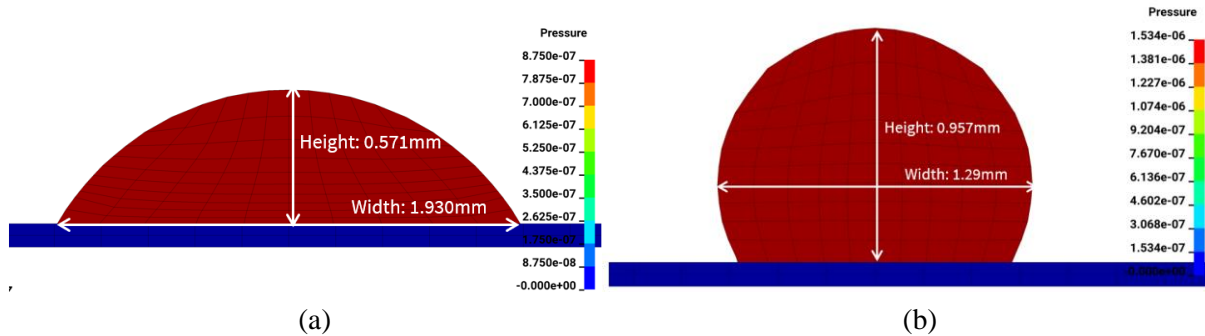


FIG. 7: Mesh section view of the final equilibrium configuration of the solder: (a) Result with equilibrium static angle $\pi/6$; (b) Result with equilibrium static angle $\pi/3$

TABLE 1: Final solder geometry with equilibrium contact angle $\pi/6$

	Analytical [mm]	ISPG predicted [mm]	Difference
Height	0.576	0.571	0.87%
Width	1.995	1.930	3.26%

TABLE 2: Final solder geometry with equilibrium contact angle $\pi/3$

	Analytical [mm]	ISPG predicted [mm]	Difference
Height	0.985	0.957	2.84%
Width	1.313	1.290	1.17%

4.2 Prediction of the Standoff Height and Width of the Solder Joints on BGA

The standoff height and the maximum width of the solder joints are very important in the design process, because they affect significantly the strength of solder joints in the reliability analysis. In general, the standoff height and the maximum width of solder joints are related to the change of solder volume. In this study, different volumes of the solder are simulated, and the predicted standoff height and maximum width are compared with the experimental result (Chou et al., 2006). The solder pad and solder mask are shown in Fig. 8. The material of solder pad is Ni-Au and the mask is made of epoxy. The equilibrium contact angles of the molten solder formed on the solder pad and mask are 5° and 148° , respectively. Five different volumes of solder are used for the simulations, and they are 0.0141mm^3 , 0.0564mm^3 , 0.1077mm^3 , 0.1218mm^3 and 0.2298mm^3 . The solders are discretized with 1365, 2299, 4389, 3355 and 3742 particles, respectively. The material properties of solder are (Chou et al., 2006): the density and surface tension of the solder are $8.93 \times 10^{-6}\text{g/mm}^3$, $4.985 \times 10^{-6}\text{kN/mm}$, respectively; the dynamic viscosity ϑ is $2.27 \times 10^{-7}\text{kN ms/mm}^2$. The gravity is $9.81 \times 10^{-3}\text{mm/ms}^3$.

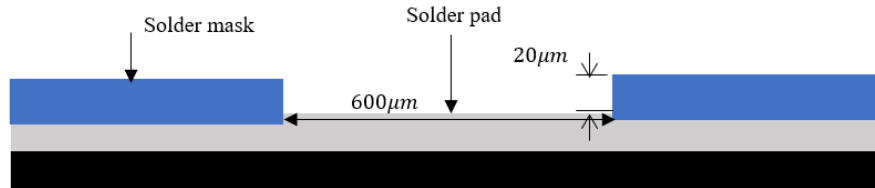
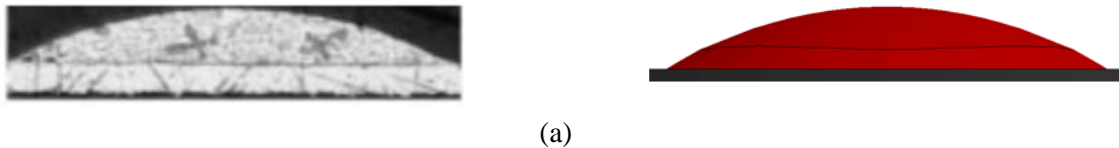


FIG. 8: The cross section of BGA substrate

Fig. 9 compares the cross sections of solder joints between experimental observations (Chou et al., 2006) and simulation results. In general, they agree very well with each other. As shown in Fig. 9, the contact angle formed in solder pads increases with the increase of solder volume.



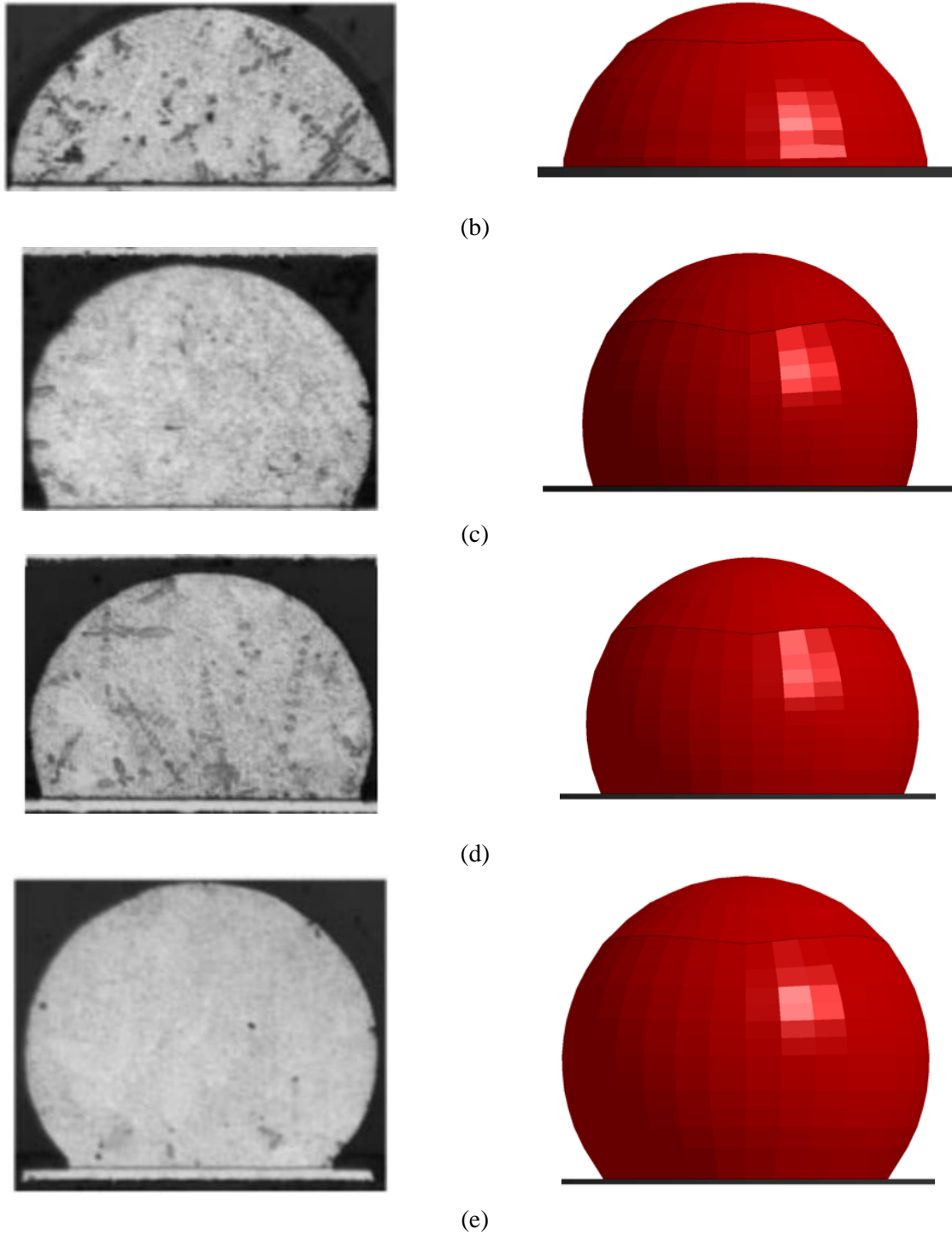


FIG. 9: Comparison on the cross sections of the solder joints between the experimental observations and the simulation results. Left: experimental observations; right: simulation: **(a)** Volume = 0.0141 mm^3 ; **(b)** Volume = 0.0564 mm^3 ; **(c)** Volume = 0.1077 mm^3 ; **(d)** Volume = 0.1218 mm^3 ; **(e)** Volume = 0.2298 mm^3

Fig. 10 compares the simulated standoff height and the maximum width of the solder joints between the simulated results and the experimental measurements (Chou et al., 2006), and the results match very well.

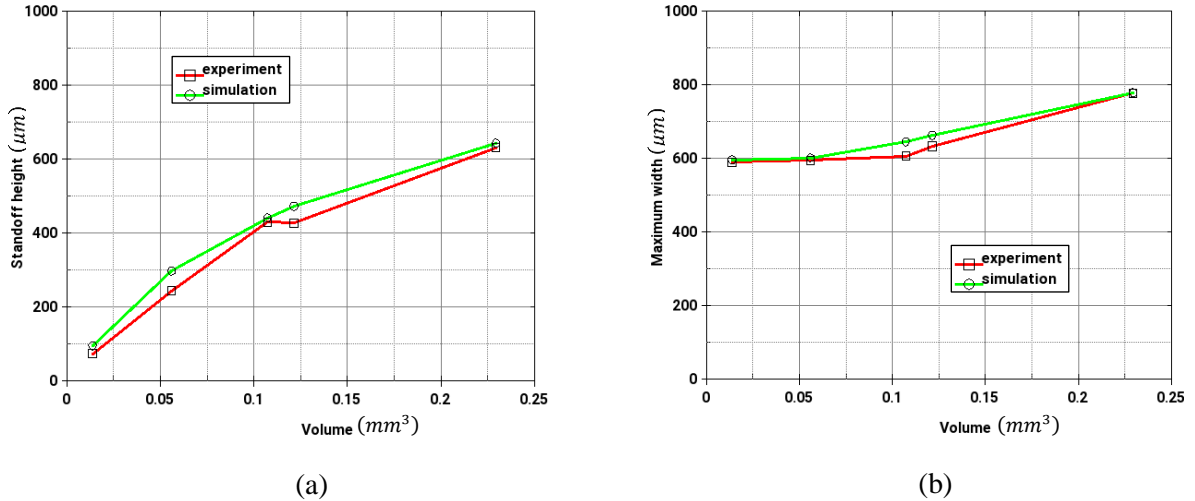


FIG. 10: Comparison of the standoff height and maximum width of the solder joints with experimental data: (a) Standoff height vs. solder volume; (b) Maximum width vs. solder volume

4.3 ISPG for Solder Ball Shape Prediction

In this example, we will investigate the assembly of BGA with solder joints. The assembly consists of 100 SAC405 solder joints shown in Fig. 11. All solders are modeled with Solder Mask-Defined (SMD) at the device. Due to symmetry of the assembly geometry, only one-quarter of the assembly is modeled, and the symmetrical boundary conditions are applied at the corresponding boundaries. The original geometries of the solder joints are modeled as cylinders with diameter of 0.48mm and height of 0.4mm. The solder will be deformed under the surface tension and the pressure of the copper traces, which are simplified as two thin plates with 0.02mm thickness. The applied velocity at the corner point of the silicon die shown in Fig. 11 is $\bar{v} = 1.6667 \times 10^{-6}$ mm/ms from 0ms to 60,000 ms, and the total displacement is 0.1 mm.

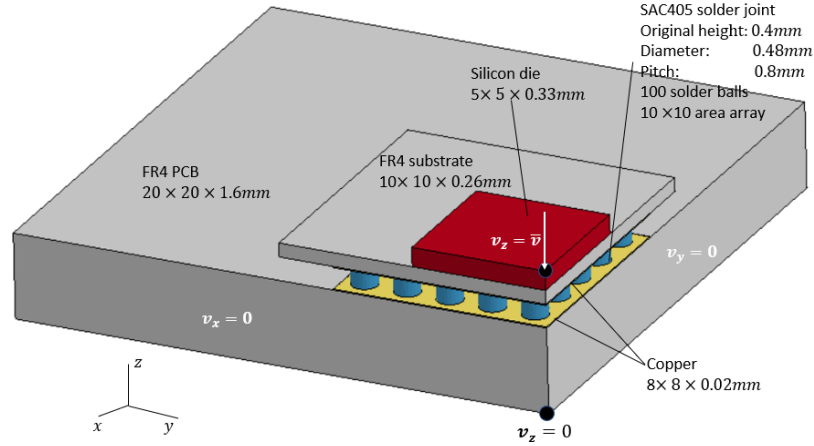


FIG. 11: Sketch view of the quarter model of the BGA assembly

The FR4 PCB, FR4 substrate, copper traces and silicon die are discretized with hexahedron element (element formulation -1 in LS-DYNA) with 0.5mm size in x and y direction, and with 4, 2, 1 and 2 elements in thickness direction as show in Fig. 12. Each solder joint is discretized with 1560 hexahedron elements and 1819 nodes, then they are transferred to ISPG elements. Finally, there are totally 49277 nodes in the model.

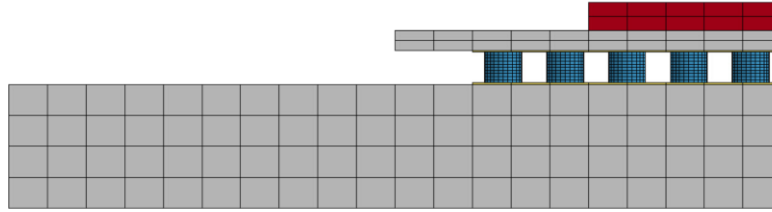


FIG. 12: Meshing of the quarter model of the BGA soldering

The initial temperature is set as 25°C, and linearly increased to 200°C from 0ms to 60,000 ms. Currently the thermal effects in the solder joints is not considered. The density and surface tension of the solders are $8.93 \times 10^{-6} g/mm^3$, $4.985 \times 10^{-6} kN/mm$, and the dynamic viscosity ϑ is $2.27 \times 10^{-7} kN ms/mm^2$. The material property of the FR4, copper trace and silicon die are listed in Tables 3-5.

TABLE 3: Material property of FR4 PCB and substrate

Poisson's ratio ν_{xy}	0.11
Poisson's ratio ν_{yz} and ν_{xz}	0.39
Thermal expansion α_x and α_y [ppm/°C]	16
Thermal expansion α_z [ppm/°C]	84
Young's modulus E_x and E_y [MPa]	27,924
Young's modulus E_z [MPa]	12,204
Shear modulus G_{xy} [MPa]	12,600

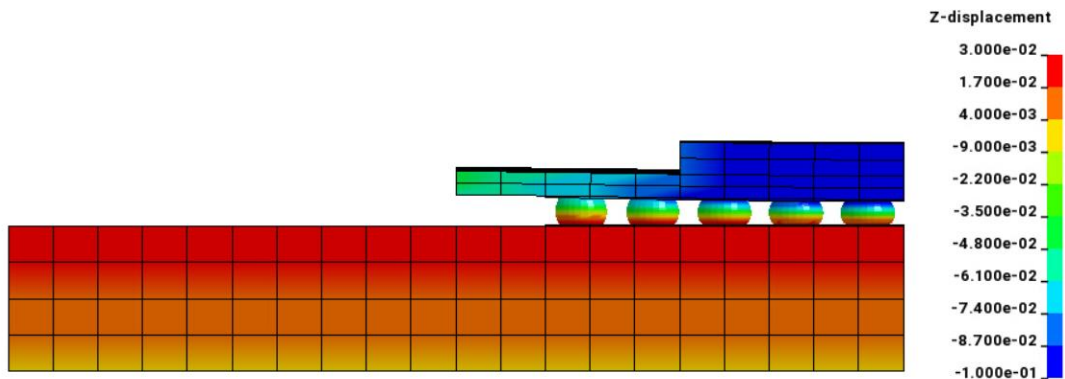
TABLE 4: Material property of silicon die

Poisson's ratio ν	0.28
Thermal expansion α [ppm/°C]	2.113
Young's modulus E [MPa]	132,460

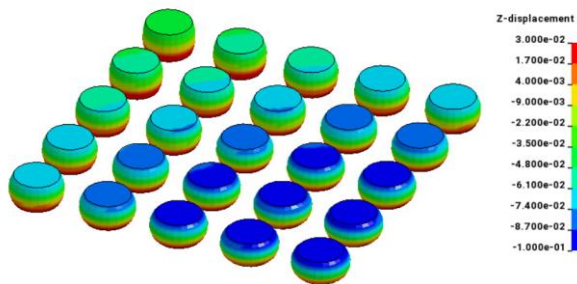
TABLE 5: Material property of copper trace

Poisson's ratio ν	0.35
Thermal expansion α [ppm/°C]	15.64
Young's modulus E [MPa]	141,920

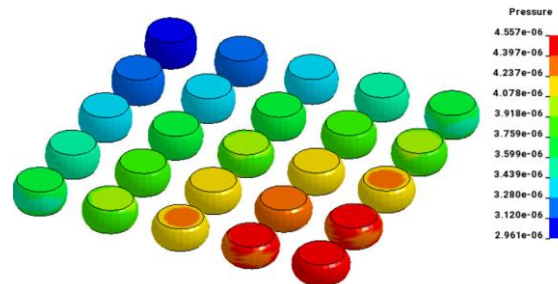
Fig. 13 (a) shows the final configuration of the BGA assembly where the warpage can be observed in the FR4 substrate, which is caused by the mismatch of the thermal expansion coefficient between the FR4 substrate and the silicon die. The warpage of the FR4 substrate leads to different geometries of the solders as shown in Figs. 13 (b) and (c) displayed in the z-displacement and pressure contours, respectively.



(a)



(b)



(c)

FIG. 13: Final configuration of the BGA assembly: (a) front view of the final deformation; (b) view of the deformed solders: z-displacement contour (mm); (c) view of the deformed solders: pressure contour (Gpa)

4.4 A PCB Package Drop Test Using Global-Local Co-Simulation

JEDEC Test Standard describes the procedures and conditions to conduct a board-level drop test on electronic packages (JEDEC Standard JESD22-B111). The PCB is mounted at each corner to a base plate that is secured to the drop table. The drop table is released to freely impact the strike table from a prescribed height. A half sine impulse is produced when the table strikes the rigid base and the impulse generates stress wave that propagates through the mounting positions of the PCB to the solder joints in the center of the board (Tamin and Shaffiar, 2014). Using the dissimilar reflowed solder ball geometries in Example 4.3, the drop shock reliability of board-level PCB package is assessed with two-scale co-simulation in this section. The characteristic deformation of solder balls is quantified and compared in two-scale co-simulation system and direct numerical simulation (DNS) method.

To produce the desired half-sine input loading, an input G method with large mass is employed in this simulation (Dhiman et al., 2008; Syed et al., 2005). In this method, a large mass element is attached to the position of the mounting holes and the acceleration is converted into force input by multiplying the acceleration with large mass. This large mass method is capable of applying acceleration on the mounting points effectively. An equivalent drop height of $H = 1.12\text{m}$ is selected and the impulse duration is 0.5ms , which corresponds to a peak acceleration of 1500G (14716 m/s^2) at time 0.25ms (Tamin and Shaffiar, 2014).

Considering the stress wave propagation from mounting points to solder joints, the deformed model of PCB assembly is extended to 200mm by 100mm in the length and width direction, respectively. The schematic view of the quarter PCB assembly in board-level drop test is shown in Fig. 14.

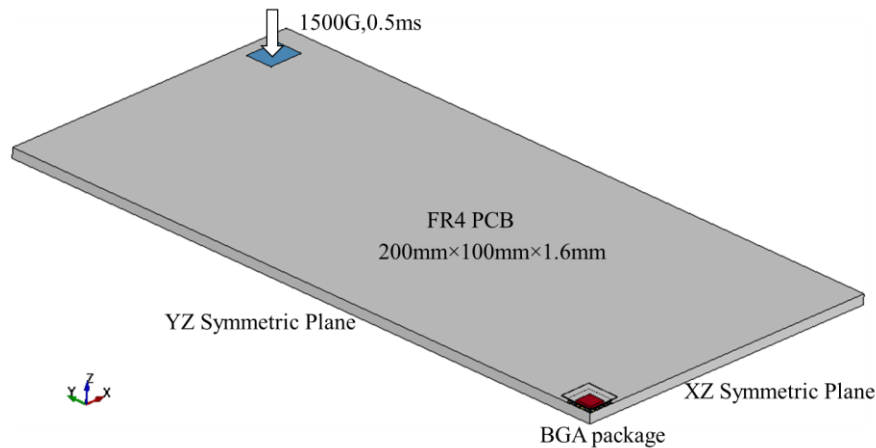


FIG. 14: Schematic view of the quarter PCB assembly for board-level drop test simulation

There are 194,611 nodes and 155,878 hexahedron elements in the whole simulation model, which is composed of macroscale model and mesoscale model as shown in Figs. 15 (a) and (b), respectively. The

macroscale model consists of FR4 PCB board and lower copper traces with 116,664 elements, while solder balls, upper copper traces, FR4 substrate and silicon die are included in the mesoscale model with 39,214 elements for detailed structural analysis. The material properties of the FR4, copper trace and silicon die follow the values in Table 3-5 without considering the thermal effect in the drop simulation. The material property of solders is identical to that in reflow analysis. **The analyses of macroscale model and mesoscale model are performed in two separated simulation jobs with information exchange using the framework shown in Fig. 5. The co-simulation duration is 1.5ms.**

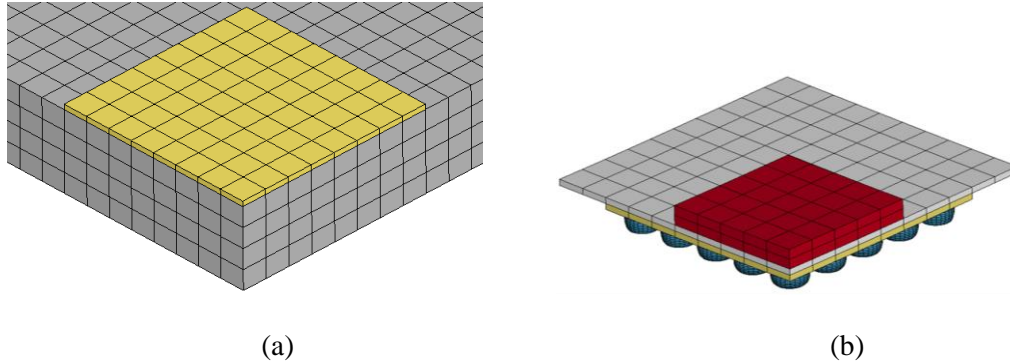


FIG. 15: Finite element mesh of macroscale and mesoscale model: **(a)** macroscale model; **(b)** mesoscale model

The predicted distribution of von Mises stress in the solder balls at $t = 1.085\text{ms}$ by two-scale co-simulation and DNS is compared in Fig. 16. Both the distribution and the magnitude of von Mises stress match very well. It is clear that the corner solder ball has the largest von Mises stress and is the most critical solder ball.

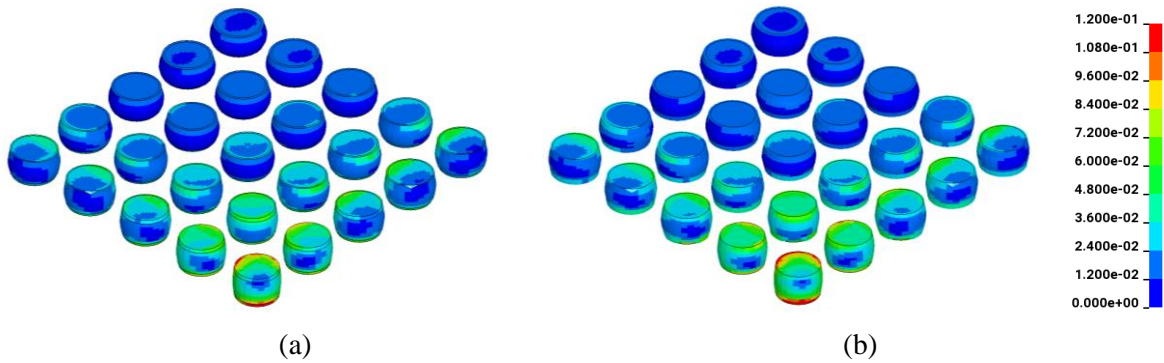


FIG. 16: Von Mises stress distribution at the upper interface of solder balls at $t = 1.085\text{ms}$: **(a)** Two-scale co-simulation (GPa); **(b)** DNS (GPa)

The displacement evolution at the center of silicon die by two-scale co-simulation and DNS is compared in Fig. 17 (a). The evolution of von Mises stress at one of elements in the most critical solder ball is also compared in Fig. 17 (b). Excepting local oscillations, the results using two-scale so-simulation

match well with DNS. An initial delay with initial input impulse is observed in both methods due to the stress wave propagation from the mounting points of PCB to the solder ball.

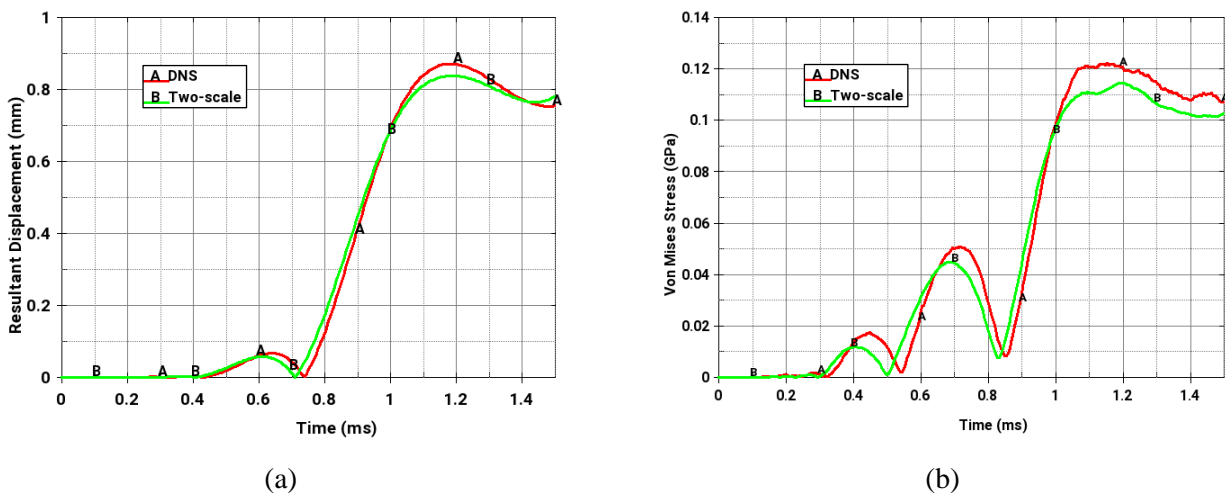


FIG. 17: Comparison of displacement and Von Mises stress evolution (a) resultant displacement at the center of silicon die; (b) Von Mises stress of the most critical solder ball

In terms of computational cost, two-scale co-simulation costs around 39 minutes with 24 CPU cores (8 for macroscale model and 16 for mesoscale model), while DNS takes around 137 minutes using the same number of CPU cores. A high efficiency can be achieved by two-scale co-simulation system with great accuracy. The Intel(R) Xeon(R) Silver 4116 CPU @ 2.10GHz is used for the computation. The comparison of normalized computation time and the CPU usage are summarized in Table 6.

TABLE 6: Comparison of normalized computation time and CPU usage

DNS	Present method
1.0	0.285
24 CPUs	8 CPUs for macroscale model + 16 CPUs for mesoscale model

5. CONCLUSIONS

Since the even increasing popularity of portable electronics, the drop shock reliability of lead-free solder joints in chip-scale packages (CSPs) has become a significant issue for the electronic industry. Today’s electronics engineers continue to search for ways to improve the reliability of lead-free solder interconnections in a drop shock event through accurate, efficient and convenient numerical simulations.

This paper presents a new computational approach that **utilizes multiple software and separate runs via co-simulation based on the bridging domain and multi-time-step techniques in explicit dynamics analysis.** It links the information of dissimilar mesoscale solder ball geometries to the macroscale drop test of a printed circuit board (PCB) for **an accurate, efficient and convenient multi-scale analysis.** Two key developments are disclosed in this study. First, a fully implicit ISPG formulation incorporating the surface tension and cohesion force terms is developed for simulating the free-surface solder reflow process. This

new method allows engineers to efficiently establish the geometry of solder ball in the mesoscale level prior to performing solder joint reliability analysis in the macroscale. Second, an explicit-explicit non-intrusive two-scale coupling method via the co-simulation technique is introduced to the two-scale system for the drop test simulation. This multiscale approach permits a new two-way coupling between the mesoscale solder joint model and macroscale chip package model for the CSPs drop shock analysis. From the best of authors' knowledge, the multiscale method has not been made available in the electronics industry for the drop shock analysis. The present approach also avoids a tedious matching mesh issue and compromises the accuracy and efficiency requirements in the industrial application.

The results in first two numerical examples reveal that the proposed implicit ISPG formation is able to accurately and efficiently predict the solder reflow profile. Unlike the existing approaches that only apply to specific solder joints, the new ISPG method provides an off-the-shelf solution to handle complex solder joint types in PCB packages. The last two numerical examples present a new multiscale simulation utilizing the reflowed solder ball shapes for the drop test of a chip-scale package. In comparison to the DNS result, the multiscale result indicates that the present method is capable of delivering an accurate and efficient solution. To further improve the accuracy of reliability analysis, the underlying microstructure of the lead-free solder ball will need to be addressed. This involves the modeling of solidification and grain growth process in reflow soldering which will be investigated in the near future.

ACKNOWLEDGMENTS

The authors wish to thank Taiwan Semiconductor Manufacturing Company (TSMC) for their support to this research.

REFERENCES

- Ahmed N. and Xue, P., Determination of the size of the local region for efficient global/local modeling in a large composite structure under impact loading, *Int. J. Impact Eng.*, in press, doi: 10.1016/j.ijimpeng.2020.103646, 2020.
- Amalu, E. H. and Ekere, N. N., High temperature reliability of lead-free solder joints in a flip chip assembly, *J. Mater. Process. Tech.*, vol. **212**, pp. 471-483, 2012.
- Asai, M., Aly, A. M., Sonoda, Y. and Sakai, Y., A stabilized incompressible SPH method by relaxing the density invariance condition, *J. Appl. Math.*, vol. **2012**, pp. 139583, 2012.
- Belytschko, T., Yen, H. J. and Mullen R., Mixed methods for time integration, *Comput. Methods Appl. Mech. Eng.*, vol. **17-18**, pp. 259-275, 1979.
- Bettinotti, O., Allix, O., Perego, U., Oancea, V. and Malherbe, B., Simulation of delamination under impact using a global-local method in explicit dynamics, *Finite Elem. Anal. Des.*, vol. **125**, pp. 1-13, 2017.
- Boucard, P. A., Odievre, D. and Gatuingt, F., A parallel and multiscale strategy for the parametric study of transient dynamic problems with friction, *Int. J. Numer. Methods Eng.*, vol. **88**, pp. 657-672, 2011.
- Brakke, K. A., The surface evolver and the stability of liquid surface, *Philos. Trans. R. Soc. London, Ser. A*, vol. **354**, pp. 2143-2157, 1996.
- Chiang, K. N., Lin, Y. T. and Cheng, H. C., On enhancing eutectic solder joint reliability using a second-reflow process approach, *IEEE Trans. Adv. Packag.*, vol. **23**, no. 1, pp. 9-14, 2000.
- Chiang, K. N. and Yuan, C. A., An overview of solder bump shape prediction algorithms with validations, *IEEE Trans. Adv. Packag.*, vol. **24**, no. 2, pp. 158-162, 2001.

- Chong, D. Y. R., Che, F. X., Pang, J. H. L., Ng, K., Tan, J. Y. N. and Low, P. T. H., Drop impact reliability testing for lead-free and lead-based soldered IC packages, *Microelectron. Reliab.*, vol. **46**, pp. 1160-1171, 2006.
- Chou, Y. Y., Chang, H. J., Kuo, J. H. and Hwang, W. S., The simulation of shape evolution of solder joints during reflow process and its experimental validation, *Mater. Trans.*, vol. **47**, no. 4, pp. 1186-1192, 2006.
- Dehning, C., Bierwisch, C. and Kraft, T., Co-simulations of Discrete and Finite Element Codes. In: Griebel M., Schweitzer M. (eds) Meshfree Methods for Partial Differential Equations VII. *Lecture Notes in Computational Science and Engineering*, vol. **100**, Springer, Cham, 2015.
- Dhia, H. B. and Rateau, G., The Arlequin method as a flexible engineering design tool, *Int. J. Numer. Methods Eng.*, vol. **62**, pp. 1442-1462, 2005.
- Dhiman, H. S., Fan, X. and Zhou, T., Modeling Techniques for Board Level Drop Test for a Wafer-Level Package, *International Conference on Electronic Packaging Technology & High Density Packaging*, 2008.
- Gendre, L., Allix, O., Gosselet, P. and Comte, F., Non-intrusive and exact global/local techniques for structural problems with local plasticity, *Comput. Mech.*, vol. **44**, pp. 233-245, 2009.
- Grovenor, C. R. M., *Microelectronic Materials*, New York: Taylor & Francis Group, 2017.
- Guermond, J. L., Mineev, P. and Shen, J., An overview of projection methods for incompressible flows, *Comput. Methods Appl. Mech. Eng.*, vol. **195**, pp. 6011-6045, 2006.
- Idelsohn, S. R., Oñate, E. and Del Pin, F., The particle finite element method: a powerful tool to solve incompressible flows with free-surfaces and breaking waves, *Int. J. Numer. Methods Eng.*, vol. **61**, pp. 964-989, 2004.
- JEDEC Standard JESD22-B111, Board Level Drop Test Method of Components for Handheld Electronic Products.
- Heinrich, S. M., Schaefer, M., Schroeder, S. A. and Lee, P. S., Prediction of solder joint geometries in array-type interconnects, *ASME J. Electron. Packag.*, vol. **118**, pp. 114-121, 1996.
- Kok, C. K., Ng, W. J., Ooi, C. C. and Liew, K. W., Ball-grid-array solder joint model for assembly-level impact reliability prediction, *Microelectron. Reliab.*, vol. **65**, pp. 184-191, 2016.
- Koshizuka, S. and Oka, Y., Moving-particle semi-implicit method for fragmentation of incompressible fluid, *Nucl. Sci. Eng.*, vol. **123**, pp. 421-434, 1996.
- Ma, H. and Lee, T. K., Effects of board design variations on the reliability of lead-free solder joints, *IEEE Trans. Compon. Packag. Manuf. Technol.*, vol. **3**, no. 1, pp. 71-78, 2013.
- Pan, X., Wu, C. T., Hu, W. and Wu, Y., A momentum-consistent stabilization algorithm for Lagrangian particle methods in the thermo-mechanical friction drilling analysis, *Comput. Mech.*, vol. **64**, pp. 625-644, 2019.
- Pan, X., Wu, C. T. and Hu, W., A semi-implicit stabilized particle Galerkin method for incompressible free surface simulations, *Int. J. Numer. Methods Eng.*, in press, doi: 10.1002/nme.6396, 2020.
- Rayasam, M., Subbarayan, T. B., Gurumurthy, C. and Wilcox, J. R., A model for assessing the shape of solder joints in the presence of PCB and package warpage, *ASME J. Electron. Packag.*, vol. **128**, pp. 184-191, 2006.
- Rodrigues, N., Ferreira, A. C., Teixeira, S. F., Soares, D., Teixeira, J. C., Cerqueira, F. and Macedo F., Contact angle measurement of SAC 305 solder: numerical and experimental approach, *J. Mater. Sci.: Mater. Electron.*, vol. **27**, pp. 8941-8950, 2016.
- Sun, W., Fish, J. and Zhang, G., Superposition of non-ordinary state-based peridynamics and finite element method for material failure simulations, *Meccanica*, vol. **55**, pp. 681-699, 2020.
- Syed, A., Kim, S. M., Lin, W., Khim, J. Y., Song, E. S., Shin, J. H. and Panczak, T., A Methodology for Drop Performance Prediction and Application for Design Optimization of Chip Scale Packages, *Electronic Components and Technology Conference*, 2005.
- Tamin, M. N. and Shaffiar, N. M., Solder Joint Reliability Assessment: Finite Element Simulation Methodology, Switzerland: Springer, 2014.
- Wu, C. T., Wu, Y., Crawford, J. E. and Magallanes, J. M., Three-dimensional concrete impact and penetration simulations using the smoothed particle Galerkin method, *Int. J. Impact Eng.*, vol. **106**, pp. 1-17, 2017.

- Wu, C. T., Bui, T. Q., Wu, Y., Luo, T. L., Wang, M., Liao, C. C., Chen, P. Y. and Lai, Y. S., Numerical and experimental validation of a particle Galerkin method for metal grinding simulation, *Comp. Mech.*, vol. **61**, pp. 365-383, 2018.
- Wu, C. T., Wu, Y., Lyu, D., Pan, X. and Hu, W., The momentum-consistent smoothed particle Galerkin (MC-SPG) method for simulating the extreme thread forming in the follow drill screw-driving process, *Comp. Part. Mech.*, vol. **7**, pp. 177-191, 2020.
- Xia, W., Xiao, M., Chen, Y. and Wu, F., Thermal warpage analysis of PBGA mounted on PCB during reflow process by FEM and experimental measurement, *Solder. Surf. Mt. Tech.*, vol. **26**, pp. 162-171, 2014.
- Yeung, B. H. and Lee, T. T., Evaluation and optimization of package processing and design through solder joint profile prediction, *IEEE Trans. Adv. Packag.*, vol. **26**, no. 1, pp. 68-74, 2003.
- Yu, D., Kwak, J., Park, S., Chung, S. and Yoon, J. Y., Effect of shield-can on dynamic response of board-level assembly, *ASME J. Electron. Packag.*, vol. **134**, pp. 031010, 2012.